JOURNAL OF GEOPHYSICAL RESEARCH, VOL. 112, B11306, doi:10.1029/2007JB004977, 2007

A three-dimensional crustal seismic velocity model for southern California from a composite event method

Guoqing Lin,[1,2] Peter M. Shearer,[1] Egill Hauksson,[3] and Clifford H. Thurber[4]

Received 6 February 2007; revised 10 July 2007; accepted 14 August 2007; published 16 November 2007.

[1] We present a new crustal seismic velocity model for southern California derived from *P* and *S* arrival times from local earthquakes and explosions. To reduce the volume of data and ensure a more uniform source distribution, we compute "composite event" picks for 2597 distributed master events that include pick information for other events within spheres of 2 km radius. The approach reduces random picking error and maximizes the number of *S* wave picks. To constrain absolute event locations and shallow velocity structure, we also use times from controlled sources, including both refraction shots and quarries. We implement the SIMULPS tomography algorithm to obtain three-dimensional (3-D) V_p and V_p/V_s structure and hypocenter locations of the composite events. Our new velocity model in general agrees with previous studies, resolving low-velocity features at shallow depths in the basins and some high-velocity features in the midcrust. Using our velocity model and 3-D ray tracing, we relocate about 450,000 earthquakes from 1981 to 2005. We observe a weak correlation between seismic velocities and earthquake occurrence, with shallow earthquakes mostly occurring in high *P* velocity regions and midcrustal earthquakes occurring in low *P* velocity regions. In addition, most seismicity occurs in regions with relatively low V_p/V_s ratios, although aftershock sequences following large earthquakes are often an exception to this pattern.

Citation: Lin, G., P. M. Shearer, E. Hauksson, and C. H. Thurber (2007), A three-dimensional crustal seismic velocity model for southern California from a composite event method, *J. Geophys. Res.*, *112*, B11306, doi:10.1029/2007JB004977.

1. Introduction

[2] Local earthquake tomography (LET) [*Thurber*, 1993] has been widely used to obtain high-resolution crustal images while simultaneously improving earthquake locations [*Thurber*, 1983]. The resulting models are useful in resolving the geological structure of the crust, performing path and site effect studies, and computing strong ground motion simulations. In addition, the relocated hypocenters provide added information on crustal structure and tectonics. Most studies have used ray theoretical methods to model *P* and *S* arrival time data because of the proven effectiveness of this approach, although in principle additional information is contained in other parts of the seismic waveforms.

[3] We apply LET to southern California *P* and *S* wave arrival time data from local earthquakes and explosions in order to derive a new crustal velocity model and improve absolute earthquake locations by correcting for the biasing effects of three-dimensional (3-D) structure. To reduce the volume of data used in the tomographic inversions while preserving as much of the information in the original picks as possible, we apply a technique we term the "composite event" method. We simultaneously solve for the locations of the composite events and the velocity structure in our study area using Thurber's SIMULPS algorithm [*Thurber*, 1983, 1993; *Eberhart-Phillips*, 1990; *Evans et al.*, 1994]. Our velocity model is similar to models from previous studies but also has some new features. The model can be used as a starting point for structural studies, earthquake locations, and ground motion calculations.

2. Data and Processing

[4] Our initial data are the phase arrival times of *P* and *S* waves from 452,943 events, consisting of local events, regional events and quarry blasts, from 1981 to 2005 recorded at 783 stations in southern California and picked by the network operators. Figure 1 shows the station locations in our study area.

2.1. One-Dimensional Relocation

[5] To obtain initial locations for these events, we apply the shrinking box source-specific station term (SSST) earthquake location method [*Richards-Dinger and Shearer*, 2000; *Lin and Shearer*, 2005] to the 452,943 catalog events using a 1-D velocity model that was used for the SHLK catalog presented by *Shearer et al.* [2005]. The SSST

[1]Scripps Institution of Oceanography, University of California, San Diego, La Jolla, California, USA.
[2]Now at Department of Geology and Geophysics, University of Wisconsin-Madison, Madison, Wisconsin, USA.
[3]Seismological Laboratory, California Institute of Technology, Pasadena, California, USA.
[4]Department of Geology and Geophysics, University of Wisconsin-Madison, Madison, Wisconsin, USA.

0148-0227/07/2007JB004977$09.00

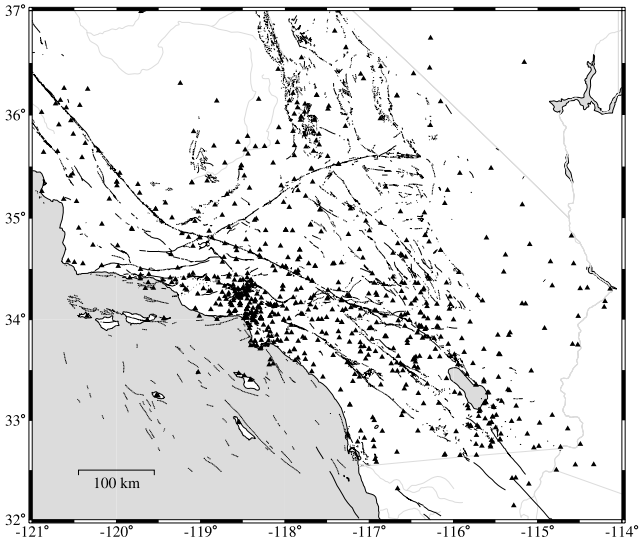

Figure 1. Locations of the 783 stations used in the study area.

approach improves the relative location accuracy among nearby events by computing spatially varying time corrections from each source region to each station, thus accounting for the correlation in residuals for closely spaced events caused by 3-D velocity structure. The shrinking box SSST algorithm is a generalization of the simple SSST method that continuously shrinks the event separation distance between the first and final iteration, which has been shown to provide some improvements in absolute location accuracy. In this study, the distance cutoff for the station term calculation is reduced gradually during the iterations from 100 km to 8 km. To avoid P_g/P_n and S_g/S_n ambiguities, we use only arrivals with source-receiver ranges of 100 km or less. We minimize the robust least squares norm, which is a hybrid l^1-l^2 misfit measure [*Lin and Shearer*, 2007], of the arrival time residuals to relocate the events with at least five picks. Figure 2 shows the relocated 428,871 events. Although the absolute location accuracy of this initial catalog is limited by the use of a 1-D model, the relative location accuracy is sufficient for us to use these locations to examine residual statistics and for the "composite event" calculations that we describe below. We did not explicitly estimate location uncertainties, but a southern California catalog computed using a similar method [*Richards-Dinger and Shearer*, 2000] yielded median horizontal and vertical standard errors in relative location of about 300 m and 700 m, respectively.

2.2. Error Estimates

[6] Before we start the tomographic inversions, we estimate the random picking errors and the scale length of 3-D heterogeneity resolvable with the arrival time data in our study area by analyzing differential residuals for pairs of events recorded at the same station. For a given pair of events, event i and event j, we compute the differential arrival time residual at a common station k after relocation as

$$dr_{ij} = r_i - r_j \tag{1}$$

$$dr_{ij} = \left(T_i^o - T_i^p - t_{0i}\right) - \left(T_j^o - T_j^p - t_{0j}\right) \tag{2}$$

where T_i^o and T_j^o are the observed arrival times for event i and j, T_i^p and T_j^p are the predicted traveltimes from the 1-D velocity model, and t_{0i} and t_{0j} are the origin times of the events after relocation. Figure 3 shows the median absolute deviation (MAD) of the differential residuals as a function of event separation distance. By plotting how differential residual variance changes as a function of event separation distance, it is possible to characterize random picking error compared to the correlated signals caused by 3-D velocity structure [e.g., *Gudmundsson et al.*, 1990]. In addition, these plots provide constraints on the scale length of the resolvable heterogeneity and the appropriate distances to use in smoothing residuals for computing source-specific station terms. In principle, as the event separation distance shrinks to zero, the differential residual will reflect random picking error alone. However, this is true only if the locations and origin times are perfectly accurate. In Figure 3 the smallest differential residuals are achieved for the source-specific station term locations, consistent with random individual picking errors of 0.02 s for P (solid curve) and 0.03 s for S (dashed curve). The differential residuals show minimal growth with event separation in Figure 3c, indicating the effectiveness of the source-specific station terms in cancelling the effects of 3-D structure. The circles and crosses in Figure 3c show the results when the SSSTs are added to the residuals; as expected the residuals grow significantly with event separation, and behave very similarly to the single event location residuals. Figure 3 also shows that the differential residual MAD increases with event separation distance, which implies that there exists some small-scale heterogeneity. This will be considered in the tomographic inversions presented below.

3. Composite Event Method

[7] In principle, we would like to use all available events and pick information in tomographic inversions, but this is computationally intensive. To reduce the volume of data, as well as to make the event distribution more uniform, it is

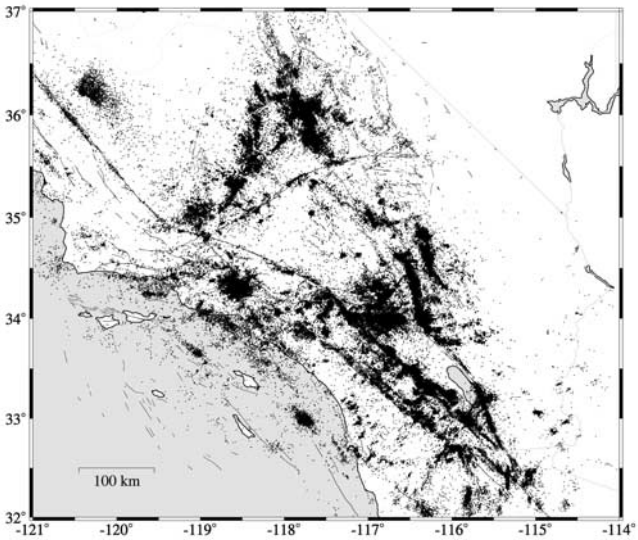

Figure 2. Locations of the 428,871 1-D relocated events using only the arrival time data in southern California from 1981 to 2005.

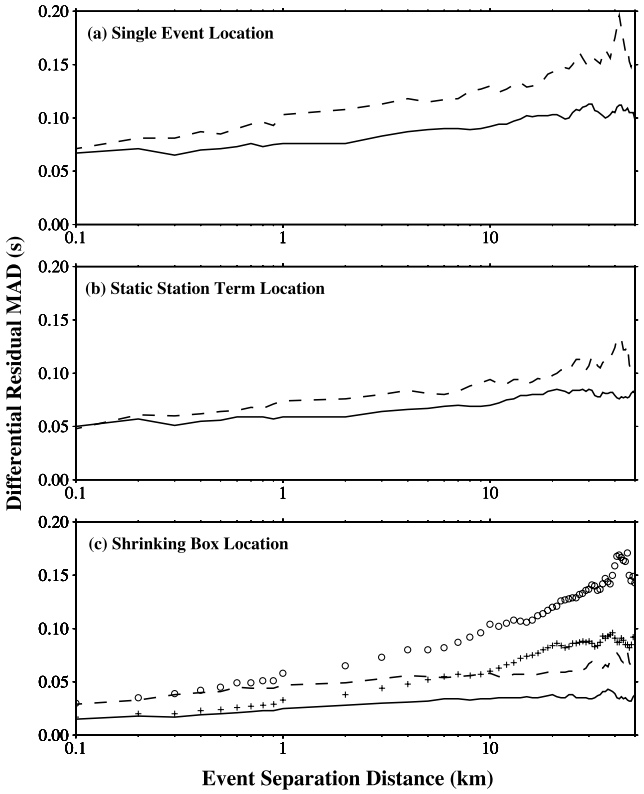

Figure 3. Differential residual median absolute deviation (MAD) for *P* picks (solid) and *S* picks (dashed) as a function of event separation distance for (a) single-event location residuals, (b) static station term location residuals, and (c) shrinking box SSST location residuals. The crosses and circles in Figure 3c are the sums of the differential residuals and the source specific station terms for (*P*) and (*S*), respectively.

common to select a spatially diverse set of master events [e.g., *Hauksson*, 2000]. However, this approach often discards the vast majority of the available picks. Here we present an approach, which we term the "composite event" method, that attempts to preserve as much of the original pick information as possible. The idea is similar to the summary ray method of *Dziewonski* [1984] and the grid optimization approach of *Spakman and Bijwaard* [2001]. We exploit the fact that closely spaced events will have highly correlated residuals in which random picking error dominates, whereas residual decorrelation caused by 3-D structure will occur mainly at much larger event separation distances.

[8] We use the 1-D shrinking box SSST locations for this method, since they provide good relative earthquake locations. Figure 4 shows how our composite event algorithm works. The triangles are the stations and the small squares are the target events. Composite events are derived from the residuals for all events within a radius of r_1 of the target event. The number of composite events is limited by requiring them to be separated from each other by a radius, r_2. We select the first target event as the one from our entire data set that has the greatest number of contributing picks from all the nearby events, shown by the stars in Figure 4 in the sphere with radius r_1 centered at the target event. The location of the composite event is the centroid of all the events in the sphere r_1. Arrival time picks for the composite event to each station that recorded any events within the sphere r_1 are the robust mean [*Lin and Shearer*, 2007] of the arrival time residuals from the individual events added to the calculated traveltime from the composite event location to the station, using the same 1-D velocity model used to locate the events and compute the residuals.

[9] This process results in composite event picks that preserve the pick information of the contributing events, and which are relatively insensitive to the assumed 1-D velocity model. Next, the events within the sphere with radius r_2 centered at this event, shown by the dots, are flagged so that they will not be treated as candidates for additional composite events. The second target event is the one among all the remaining events that has the greatest number of contributing picks from all the nearby events in the sphere with radius r_1, then again the events within the sphere with radius r_2 centered at this event are flagged, and so on.

[10] The total number of composite events depends on the size of r_2, and the number of contributing picks on the size of r_1. In our study, considering the computational requirements of our planned tomographic inversions, the scale length of 3-D heterogeneity resolvable with arrival time data in our study area, and the desired composite event distribution, we use 2 km for r_1, 6 km for r_2 and constrain each composite event to have more than 20 picks with at least 5 *S* picks. This results in 2,597 composite events consisting of 109,460 composite *P* picks and 53,549 composite *S* picks, while the number of total contributing *P* picks is 2,293,728 and *S* picks is 575,769. In other words, 0.6% of the total events, the 2597 composite events, preserve most of the information of 38% of the original picks (7.75 million picks). The composite events are shown in Figure 5a by the dots.

[11] We have found that the resulting composite event picks are not very sensitive to changes in the 1-D velocity model used to compute the individual event locations, because most of the effect of pick bias from the 1-D velocity model will be absorbed into the source-specific station terms, and that their residuals are highly correlated to the residual patterns from single events. In Figure 6, we show

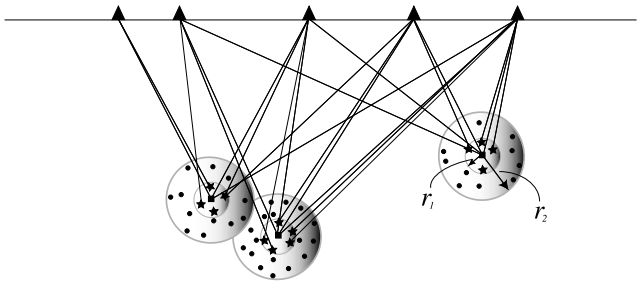

Figure 4. Cartoon showing how our composite event algorithm works. Triangles represent the stations. Squares represent the target events, and stars represent the nearby events around the targeted composite event in a given radius r_1, which provide additional traveltime information for the composite events. Dots represent the events excluded from consideration as future composite events after we choose each composite event. See text for more details.

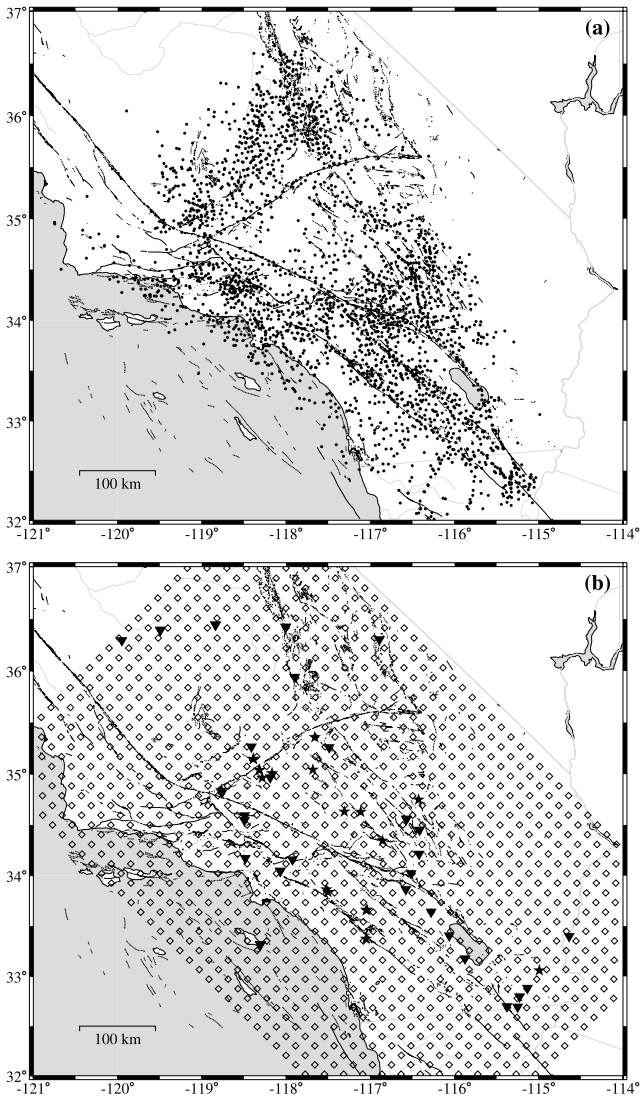

Figure 5. (a) The 2597 composite events (dots). (b) The 15-km grid points (diamonds) for our tomographic inversion. Stars represent the 19 quarries, and inverted triangles represent the 36 shots, which are used in the tomographic inversion to constrain absolute event locations and shallow velocity structure.

residual comparisons between single events and composite events at common stations for 2 randomly chosen events. The patterns of both *P* and *S* residual distributions are very similar between the single and composite events. This confirms that the arrival time picks of our composite events carry the same information as the contributing events, which we will solve for in our tomographic inversions. The advantage of using composite events rather than single master events is that the random picking error is reduced by averaging picks from many nearby events and that the maximum possible number of stations can be included for each event (i.e., generally no single event has picks for all of the available stations). This is particularly valuable for maximizing the number of *S* picks, which are picked relatively infrequently by the network operators and total only about 26% of the number of *P* picks in the complete data set. The composite event method yields almost three times the number of picks than simply selecting the one with the most picks in each sphere. The reduction in random picking error depends upon the number of picks that contribute to each composite pick. The median number of contributing picks is 18, which corresponds to a 76% reduction in random picking error, assuming Gaussian statistics.

4. Controlled Sources

[12] Because of the trade-off between earthquake locations and velocity structure in the tomography problem, controlled sources are often used in velocity inversions to

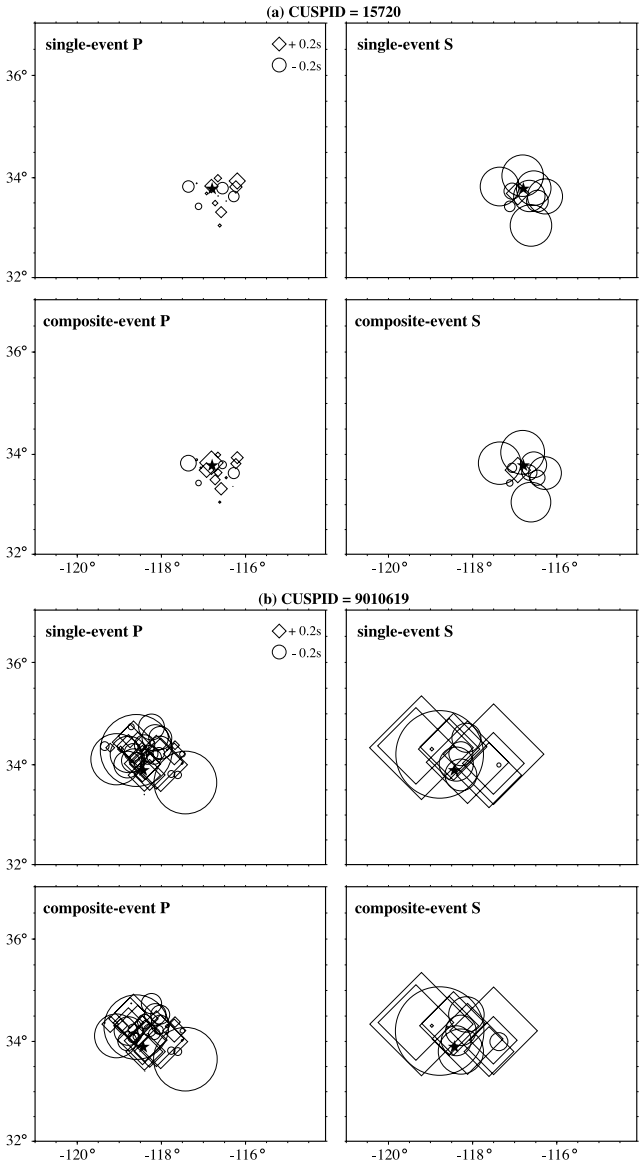

Figure 6. Arrival time residual comparison between single events and composite events. We show residuals from both the catalog event and the composite event for two randomly chosen events at common stations. The similar residual patterns confirm that the arrival time data of our composite events carry the same information as the contributing events, which we will solve for in our tomographic inversions.

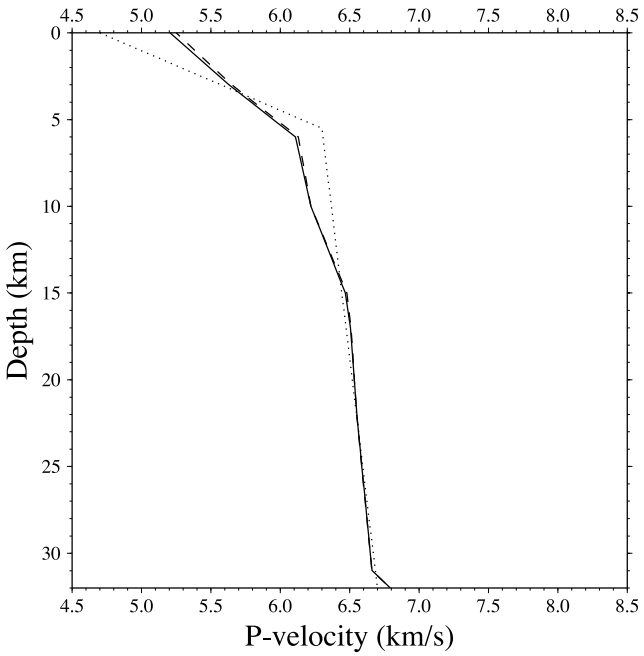

Figure 7. *P* velocity models as a function of depth: the 1-D starting model (dotted line), the 3-D starting model (dashed line), and the final model (solid line).

provide absolute reference locations for 3-D velocity models and to constrain the shallow crustal structure. Two types of controlled sources are typically used: quarry blasts and shots. Quarry blasts are man-made explosions of known location but unknown origin time, while shots also have known origin times. Our study also includes arrival times from 36 shots recorded by the Southern California Seismic Network (SCSN) and 19 quarries [see *Lin et al.*, 2006, Figure 6]. The phase data for the 19 quarries are obtained using the composite event method from the pick information for 16,574 individual events flagged as quarry blasts by the SCSN. The controlled sources in our study are plotted as the inverted triangles and stars in Figure 5b.

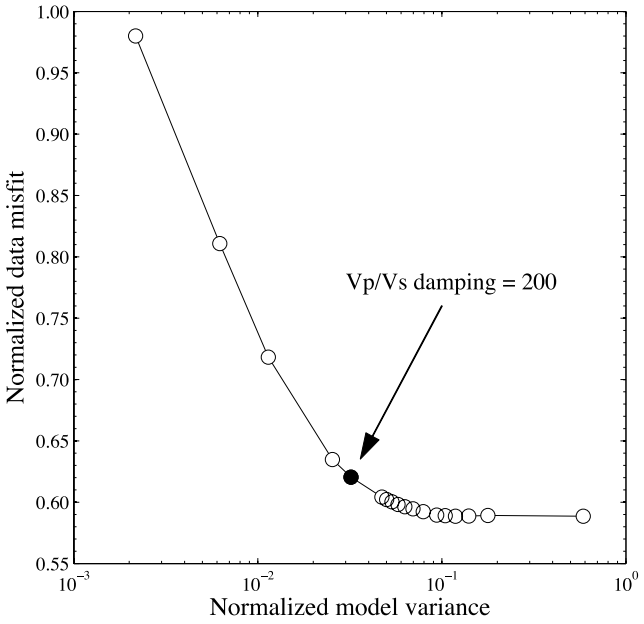

Figure 8. Trade-off curve between data misfit and model variance for V_p/V_s while damping for V_p is held at 800.

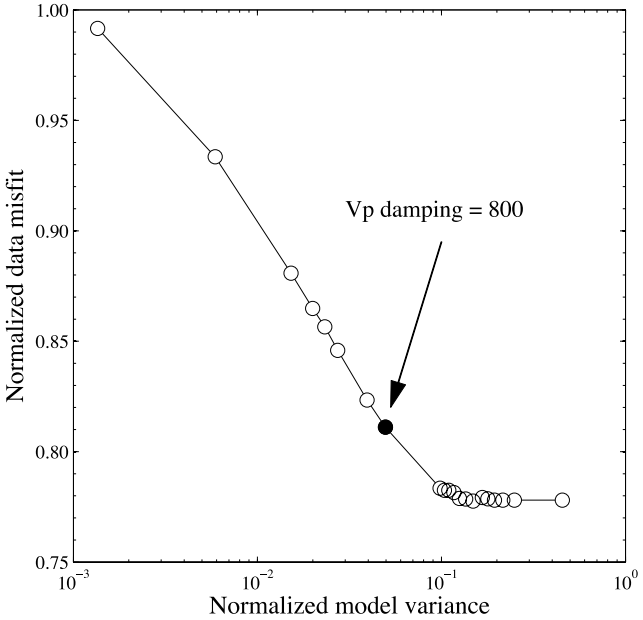

Figure 9. Trade-off curve between data misfit and model variance for V_p while damping for V_p/V_s is held at 200.

5. Three-Dimensional Simultaneous Earthquake Locations and Tomography

5.1. Inversion Method

[13] We apply the inversion method and computer algorithm SIMULPS developed by *Thurber* [1983, 1993] and *Eberhart-Phillips* [1990] (documentation provided by *Evans et al.* [1994]). SIMULPS is a damped least squares, full matrix inversion method intended for use with natural local earthquakes, with (or without) controlled sources, in which *P* arrival times and *S-P* times are inverted for earthquake locations, V_p, and V_p/V_s variations. The algorithm uses a combination of parameter separation [*Pavlis and Booker*, 1980; *Spencer and Gubbins*, 1980] and damped least squares inversion to solve for the model perturbations. The appropriate damping parameters are found using a data variance versus model variance trade-off analysis. The resolution and covariance matrix is computed in order to estimate the resolution of the model and the uncertainties in the model parameters.

5.2. Velocity Model Parameterization

[14] We find that the resulting 3-D models depend significantly on the 1-D starting model, an issue that is well recognized in seismic tomography [*Kissling et al.*, 1994]. Our strategy to reduce this dependence is to first use SIMULPS to derive a best fitting 1-D model using our 1-D location velocity model as a starting model (shown by the dotted line in Figure 7), and then use the resulting 1-D model (shown by the dashed line in Figure 7) as the starting model for the 3-D tomographic inversions. The depths of the grid points are 0, 3, 6, 10, 15, 17, 22, and 31 km. The

Table 1. Parameters for Our 3-D Velocity Models

Parameter	Value
Grid, km	15
V_p damping	800
V_p/V_s damping	200
Data variance initial, s^2	0.1236
Data variance final, s^2	0.0412
Model variance V_p, km/s^2	0.02904
Model variance V_p/V_s	0.00137

17-km point is selected to permit a relatively sharp velocity increase to occur near 16 km, which has been observed in some studies [e.g., *Hadley and Kanamori*, 1977] and which may correspond to the transition to a lower crust of predominantly mafic composition. The starting V_p/V_s ratio is 1.78, which is the average crustal V_p/V_s ratio in southern California [*Zhu and Kanamori*, 2000]. In order to test the sensitivity of the velocity model to the initial V_p/V_s ratio, we also used 1.73 as the starting value of the V_p/V_s ratio and found that the model is very similar to the one using 1.78 and fits the data almost the same. We start with the horizontally uniform layered model (shown by the dashed line in Figure 7) to invert for a 3-D model using a 15-km horizontal grid. While in principle the 6-km spacing among our composite events would permit resolving features smaller than 15 km, we were limited by our available computer power to a 15-km grid spacing. The gridding of our 3D model is 2 to 9 km vertically (an average of 4.5 km) and 15 km horizontally, and damping is also applied for stability. Thus the model will not be able to image sharp ($\sim$1 km) velocity contrasts regardless of the composite event separation.

5.3. Misfit Versus Model Variance Trade-Off Curve

[15] In order to choose an optimal damping parameter for V_p and the V_p/V_s ratio, we ran a series of single-iteration inversions with a large range of damping values, and plotted data misfit versus model variance for these runs [e.g., *Eberhart-Phillips*, 1986, 1993]. We chose damping for V_p with a trade-off curve while holding V_p/V_s damping fixed at a large value so that the effect of the S data would be as small as possible. We found that the data misfit is not as sensitive as the model variance to the damping parameter. We chose 800 as the SIMULPS damping value for V_p, which produced a good compromise between data misfit and model variance. Similarly, we chose damping for V_p/V_s while holding V_p damping fixed at 800. Figure 8 is the trade-off curve for the V_p/V_s ratio. The value we use in our tomographic inversions is 200. In order to verify that 800 is an appropriate damping value for V_p, we ran another series of single iterations with a range of V_p damping values while keeping V_p/V_s damping as 200. Figure 9 shows this trade-off curve, in which 800 is above the minimum misfit level, which means we have selected a relatively smooth model. However, since the data variance is not very sensitive to the damping values, we prefer this conservative choice of damping for V_p. Nonetheless, it should be recognized that the final appearance of our model and the amplitudes of the velocity anomalies depend strongly upon the strength of the applied damping. Models with sharper features and higher-amplitude anomalies exist that can fit the data equally well (or even slightly better), but these features would have higher uncertainty than those in smoother models. We estimate that about 50% of the changes between our new velocity model and that of *Hauksson* [2000] are caused by the stronger smoothing in our model. Some of the specific differences between the two models are discussed in detail in section 6.

6. Three-Dimensional Velocity Model Results

[16] We performed our inversions in two different stages, both with and without station terms. To avoid projecting resolvable shallow velocity structure into the station corrections, we solved for an initial model without using station terms in 4 iterations of the SIMULPS algorithm. We used this model as a starting point for 4 subsequent iterations in which we computed station terms with respect to the current 3-D model to limit the influence of rapid near-surface velocity variations (i.e., too sharp to be modeled with our 15-km grid and our damping parameters) on deeper parts of the model. Table 1 presents the parameters used in our tomographic inversions. Figure 10 shows the histograms of arrival time residuals for the composite events. The MAD residual value is reduced from 0.173 s for the 1-D starting model to 0.076 s after simultaneous tomography and relocation.

6.1. V_p Model

[17] Figure 11 shows the V_p perturbations relative to the layer-averaged velocities in the first 6 layers. The SIMULPS algorithm provides the resolution matrix, which gives an indication of how well resolved the velocity is at each grid point. The values of the resolution throughout the grid space could be increased by decreasing the damping parameter, but the velocity results may be less reliable. The black contours in the map views enclose the resolved areas with the resolution diagonal element more than 0.1, while 1.0

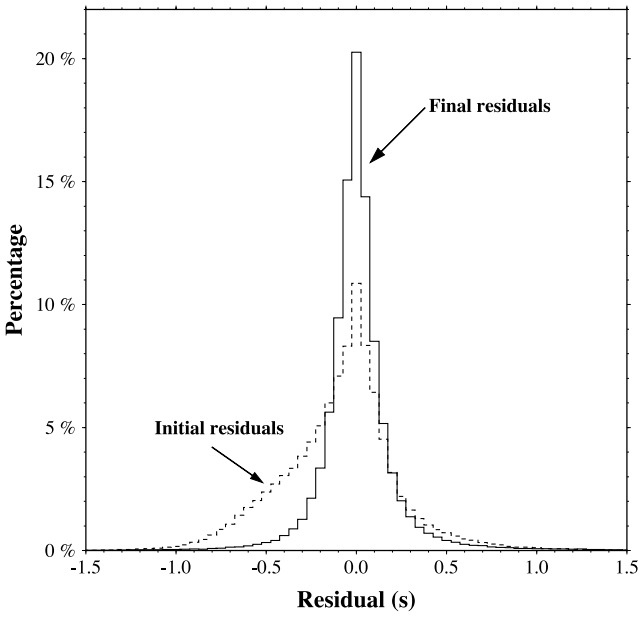

Figure 10. Histogram of arrival time residuals for the composite events, showing results before and after simultaneous location and tomography.

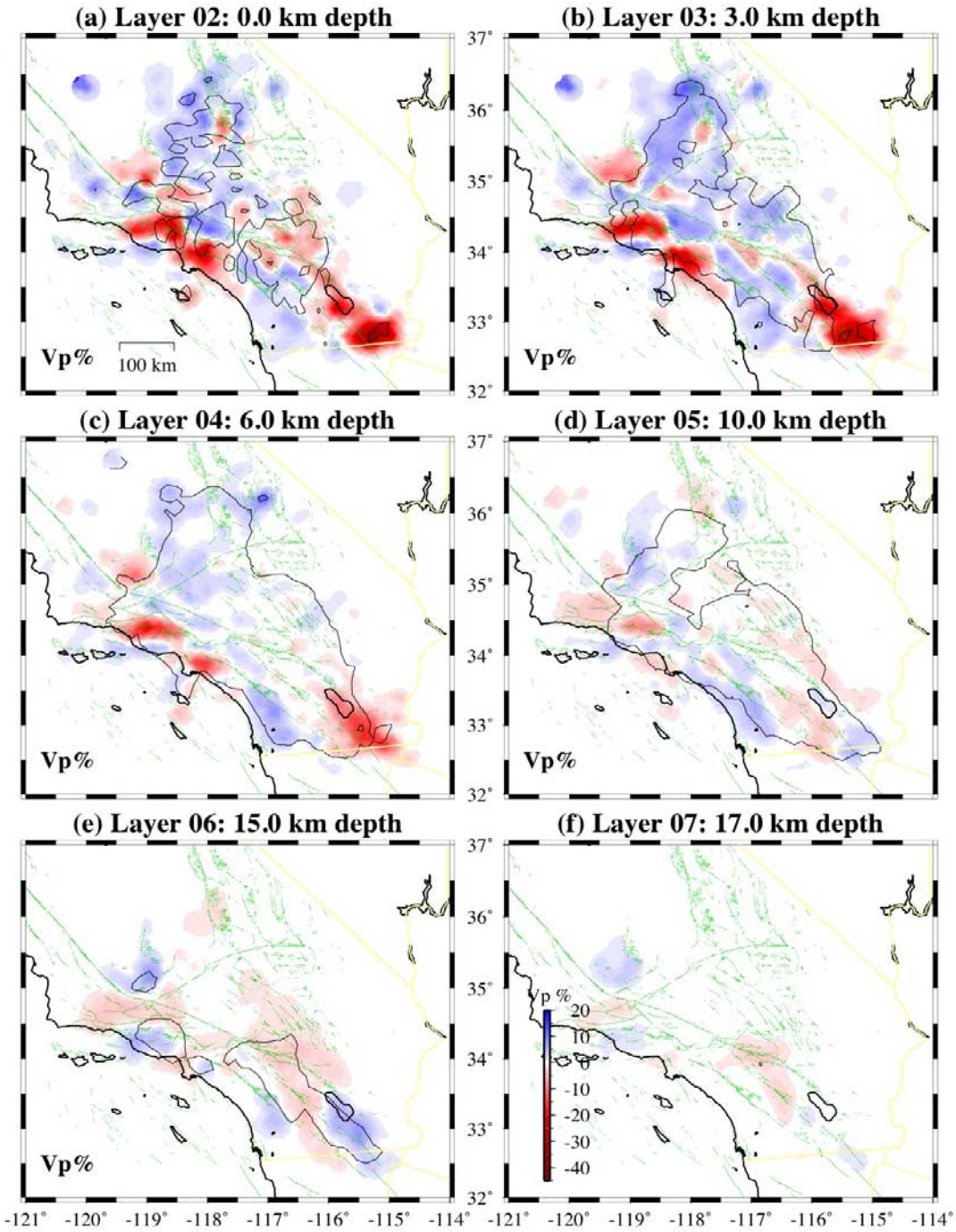

Figure 11. *P* velocity perturbations relative to the average velocity in each layer after smoothing. The black contours circle the area that we are able to resolve with the resolution above 0.1.

represents the best resolution. The top two layers of our V_p model at 0 and 3 km depth have V_p changes of relatively small spatial length of about 30 km, reflecting the near-surface geology such as bedrock outcrops and late Quaternary sedimentary deposits. In particular, the velocities in these two layers are correlated with the surface geological features. The basin areas, such as the southern San Joaquin Valley, the Ventura Basin, the Los Angeles Basin and the Imperial Valley show low-velocity anomalies, while the major mountain ranges, such as the Coast Ranges, the Transverse Ranges, the San Gabriel Mountains, and the Peninsular Ranges show higher velocities. In the 6-km depth layer, the velocity anomalies seen at the surface are still visible but become less prominent. In the middle crust (10 km), some of the features seen at shallower depths are reversed. For example, the Imperial Valley shows high velocity anomalies and the Transverse Ranges are underlain by low velocity anomalies. In the lower crust (15 km and 17 km), although the resolved areas are small, the Ventura Basin, the Los Angeles Basin, the Imperial Valley, and the

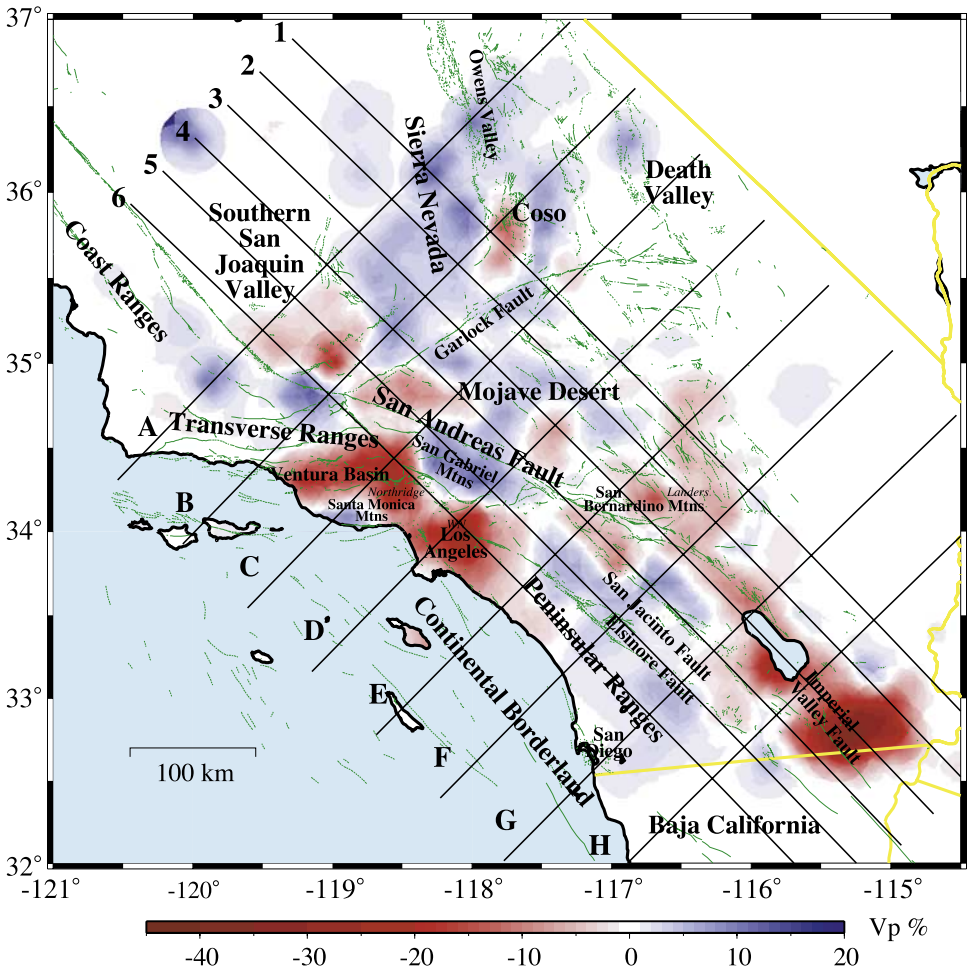

Figure 12. Some geological features in our study area and the depth profiles shown by the black straight lines for the following cross section views. The SW-NE direction profiles (shown by A, B, C, D, E, F, G, and H) are across the San Andreas fault; and the NW-SE direction profiles (shown by 1, 2, 3, 4, 5, and 6) are parallel to the San Andreas fault. The V_p perturbations in the first layer (0 km depth) are also shown.

southern San Joaquin are dominated by high-velocity anomalies, whereas the Transverse Ranges, the San Gabriel Mountains and the San Bernardino Mountains all show low velocities. The Peninsular Ranges, however, always show high velocity in each layer. The reversal of the velocity anomalies associated with most of the major basins may be related to the fact that these basins have a history of subsidence, which could be driven in part by isostatic response if there is a positive density anomaly in the lower crust beneath the basins. In fact, recent larger-scale tomography in northern California [*Zhang et al.*, 2006] has shown that the Great Valley is almost completely underlain by a high-density ophiolite body that has the same shape as the valley, suggesting that the valley shape and its subsidence may have in part been controlled by the lower crust. Our V_p model is very similar to the one by *Hauksson* [2000] except that the low-velocity anomalies in the basin areas extend to depths of about 10 km in our model (in particular, the Ventura Basin, the Los Angeles Basin, and the Imperial Valley), whereas the corresponding anomalies are present to only about 5 or 6 km in the *Hauksson* [2000] model.

[18] We present two kinds of cross section profiles of our model. These profiles are shown in Figure 12. One set is across the San Andreas fault from SW to NE shown by the straight lines marked with letters (e.g., A, B,. . ., H) and the other set is parallel to the San Andreas fault from NW to SE shown by the numbers (e.g., 1, 2, . . ., 6). Figure 12 also shows some geological features in our study area and the V_p perturbations in the first layer in our model (same as Figure 11a).

[19] The cross sections of our P velocity model for the profiles A, B, C, D, E, F, G and H are shown in Figure 13. The values of distances decrease from the SW starting point to the NE ending point. The black contours enclose our resolved area with the resolution above 0.1. We also plot the background seismicity within ±10 km of the profiles shown by the black dots. It is apparent that the resolution is the best where earthquakes are well distributed, and the resolution below 15 km depth is generally low except where there are deeper earthquakes. Again the correlations between the velocities in the shallower layers of our model with the surface geological features are seen in these cross sections.

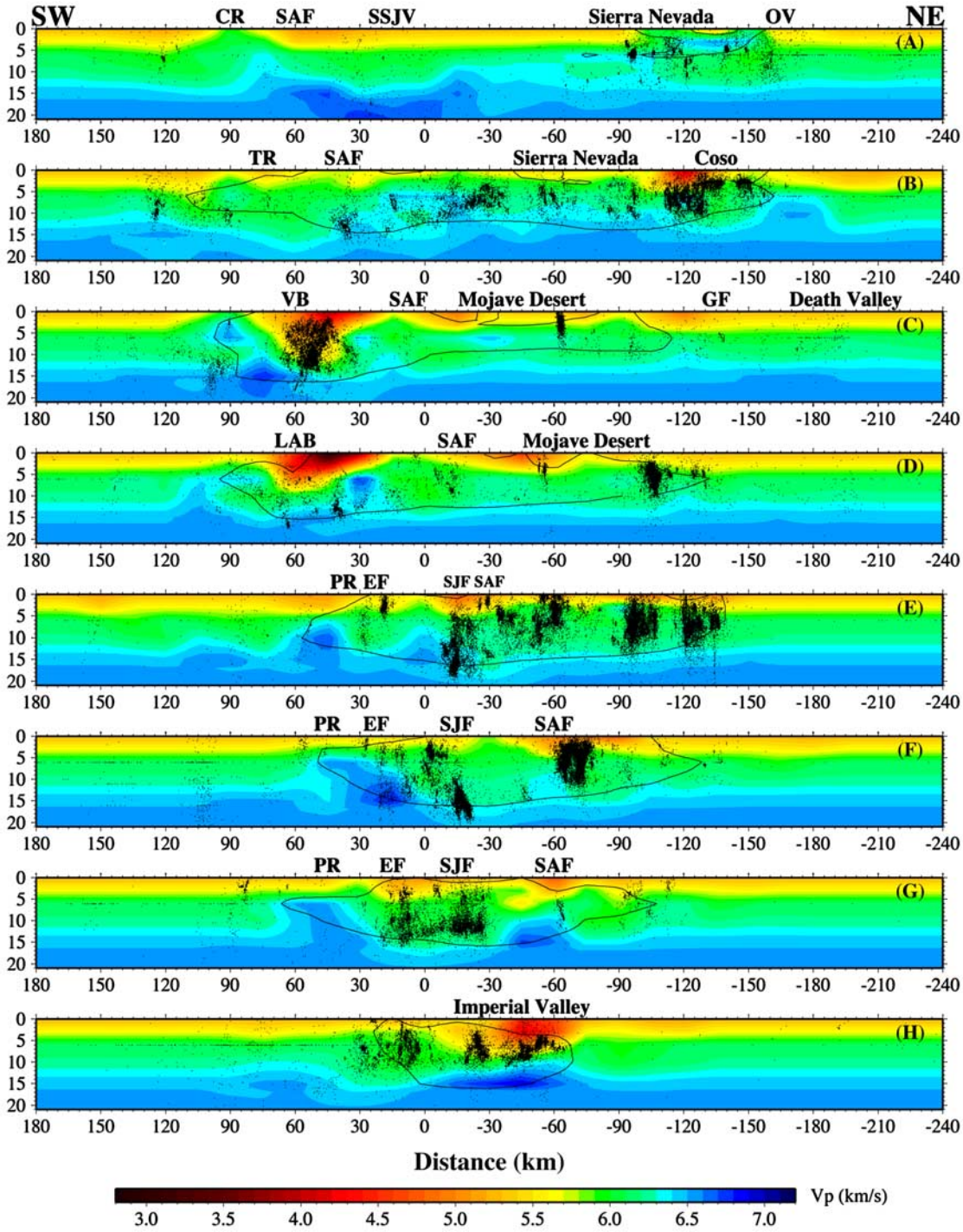

Figure 13. Cross sections through our V_p model along the SW-NE profiles shown in Figure 12 by letters, including the background seismicity (black dots) within ±10 km distance of the profile line. The black contours enclose the regions with the resolution above 0.1. The vertical exaggeration is 2. Abbreviations are CR, Coast Ranges; SAF, San Andreas Fault; SSJV, Southern San Joaquin Valley; OV, Owens Valley; TR, Transverse Ranges; VB, Ventura Basin; GF, Garlock Fault; LAB, Los Angeles Basin; PR, Peninsular Ranges; EF, Elsinore Fault; SJF, San Jacinto Fault.

Low-velocity anomalies are pronounced in the basin regions, such as the Ventura Basin in profile C, the Los Angeles Basin in D and the Imperial Valley in H, whereas relatively higher velocities are seen at the mountain ranges, such as the Coast Ranges in A and the Peninsular Ranges in E, F, and G. The very low velocities at depths to about 3 or 4 km are indicative of sediments. As shown in the map views, velocities are relatively low in many of the basin

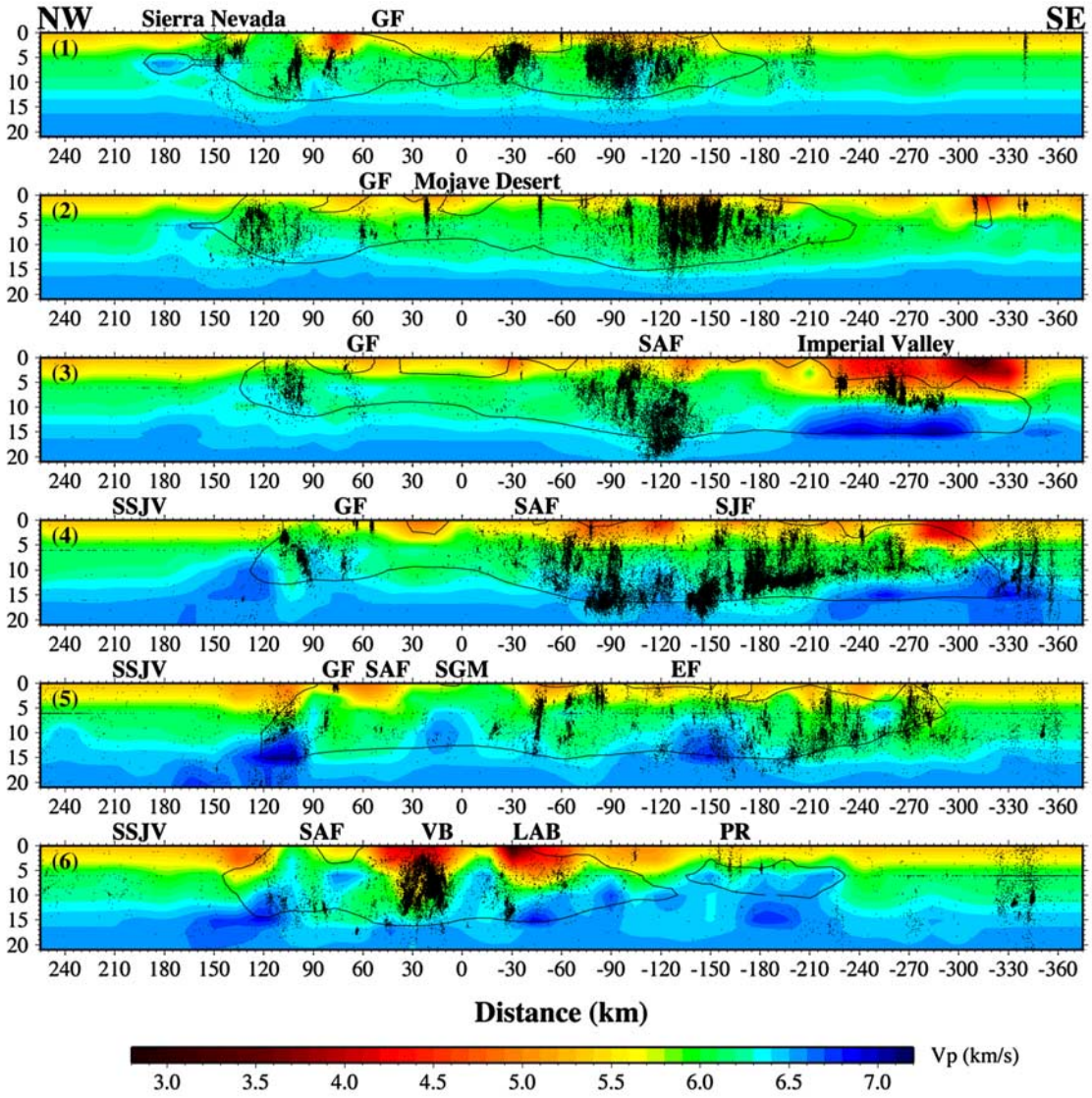

Figure 14. Cross sections through our V_p model along the NW-SE profiles shown in Figure 12 by numbers, including the background seismicity (black dots) within 10 km distance of the profile line. The black contours enclose the regions with the resolution above 0.1. The vertical exaggeration is 3. SGM is short for San Gabriel Mountains. Other geographical and fault names are the same as in Figure 13.

areas to about 10 km depth. We tend to image relatively fast regions in the deeper crust immediately below the lower-velocity anomalies in the shallower layers. Similar features are seen in the *Hauksson* [2000] model, except that the low-velocity anomalies only extend to about 5 or 6 km depth in that model. The Coso volcanic area in B is underlain by low velocities to about 5 km depth and the Southern Sierra Nevada is imaged by relatively high velocities. The Peninsular Ranges are always underlain by high velocities and the velocity increase with depth in the nearby regions is much faster relative to other areas.

[20] Figure 14 shows the cross sections of our V_p model for the profiles 1, 2, 3, 4, 5 and 6 in Figure 12, which are parallel to the San Andreas fault direction from NW to SE. The numbers of the profiles increase from the east side of the San Andreas fault to its west side and analogous features to those in Figure 13 are seen. These patterns are also very similar to those in the *Hauksson* [2000] model, except that the lowest velocity in the Imperial Valley occurs along profile 3 in our model, whereas it would be along profile 4 in Hauksson's model. This may be due to the different gridding scheme used in the two models.

6.2. V_p/V_s Model

[21] We plot absolute V_p/V_s ratios at each layer depth in Figure 15. Because of the even distribution of our composite events and the constraints on the number of picks, the areal extent of our V_p/V_s model is nearly as good as the V_p model. Again the well-resolved parts are enclosed by the 0.1 resolution contours. Even though our SIMULPS damping parameter is 200, the V_p/V_s model has comparable resolution to the V_p model, indicating that our composite event

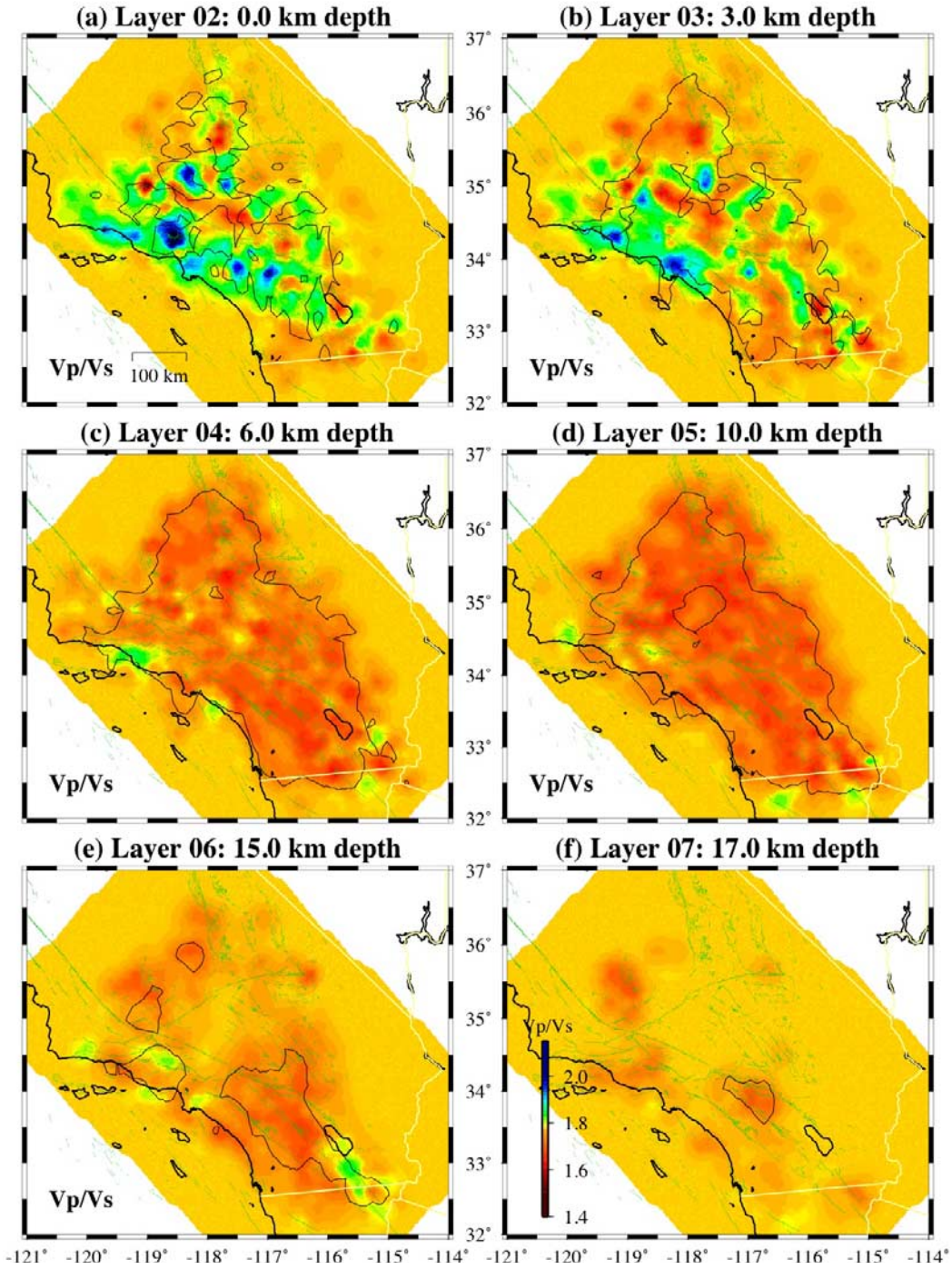

Figure 15. Absolute V_p/V_s values in each layer after smoothing. The black contours circle the area that we are able to resolve with the resolution above 0.1.

method has succeeded in obtaining sufficient *S* picks over a large region.

[22] The starting V_p/V_s model is 1.78, which is slightly higher than the common value, 1.73, for earthquake location studies in southern California. As we discussed in section 6.1, this choice did not affect our results. From the map view in Figure 15, we observe both the short spatial length variations at shallower depth and a slight decrease in average V_p/V_s compared to the starting model. The overall V_p/V_s ratio in our model ranges from 1.2 to 2.3. Two grid points contain V_p/V_s ratios of about 1.2 (at 0 km depth in the Southern San Joaquin Valley region) and 1.3 (at 3 km depth in the Imperial Valley area), which are physically unrealistic and are probably due to artifacts in our data or velocity inversions. All the other grid points have V_p/V_s values above 1.4.

[23] Our V_p/V_s model looks quite different than the *Hauksson* [2000] model, probably due to our higher starting

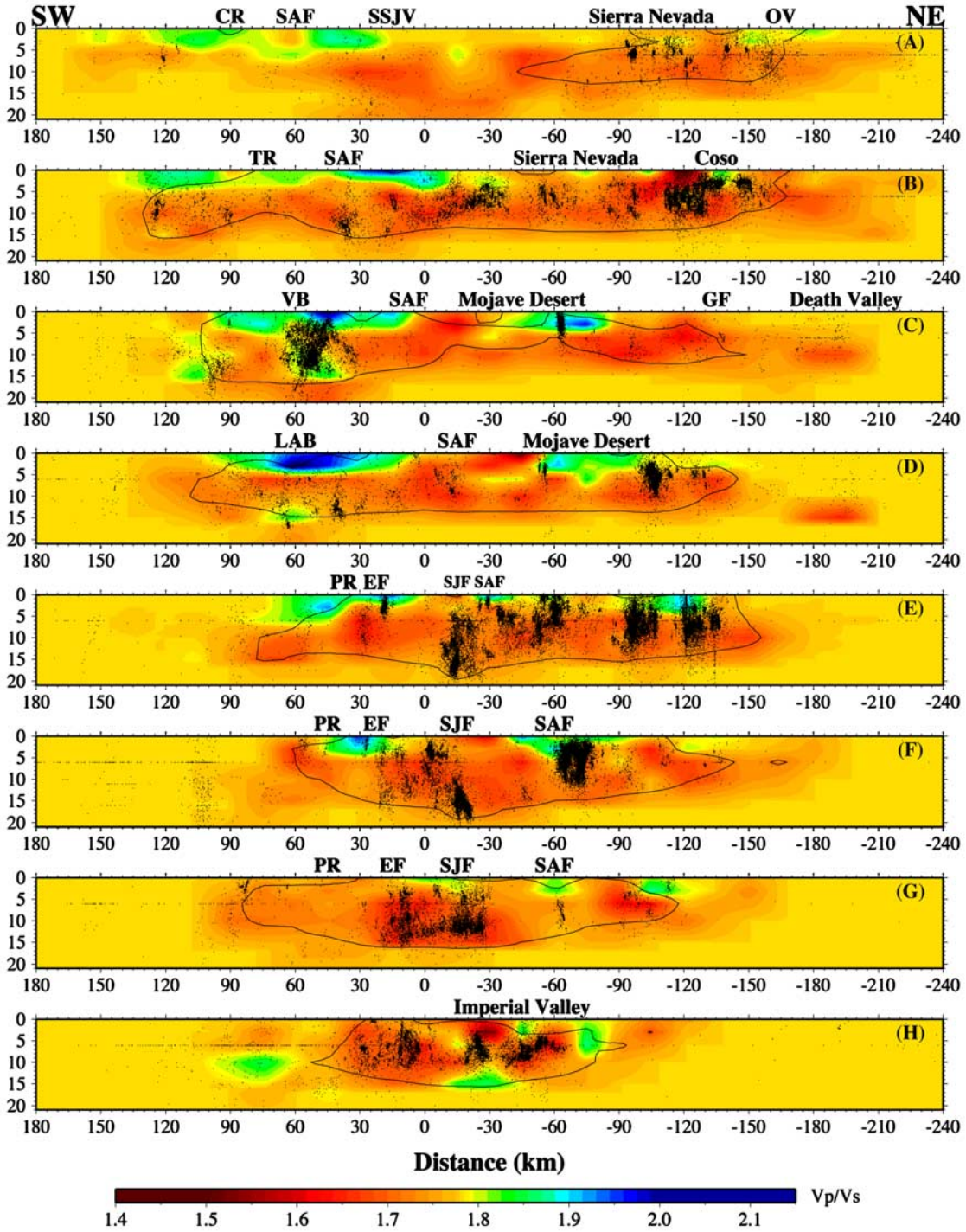

Figure 16. Cross sections through our V_p/V_s model along the SW-NE profiles shown in Figure 12 by letters, including the background seismicity (black dots) within 10 km distance of the profile line. The black contours enclose the regions with the resolution above 0.1. The vertical exaggeration is 2. The geographical and fault names are the same as in Figure 13.

V_p/V_s value, larger damping parameters and different data sets. In the first two shallow layers (0 and 3 km), we see relatively small-scale V_p/V_s anomalies. The basin areas, such as the Southern San Joaquin Valley, the Ventura Basin, the Los Angeles Basin, and the Imperial Valley, are imaged by higher anomalies in V_p/V_s values. With the corresponding lower P velocities in these regions, these features are consistent with fluid-saturated sediments. In contrast, the San Gabriel Mountains and the Peninsular Ranges show low V_p/V_s values and high V_p anomalies. We do not see the higher V_p/V_s values around the Peninsular Ranges and in Baja California seen in the *Hauksson* [2000]

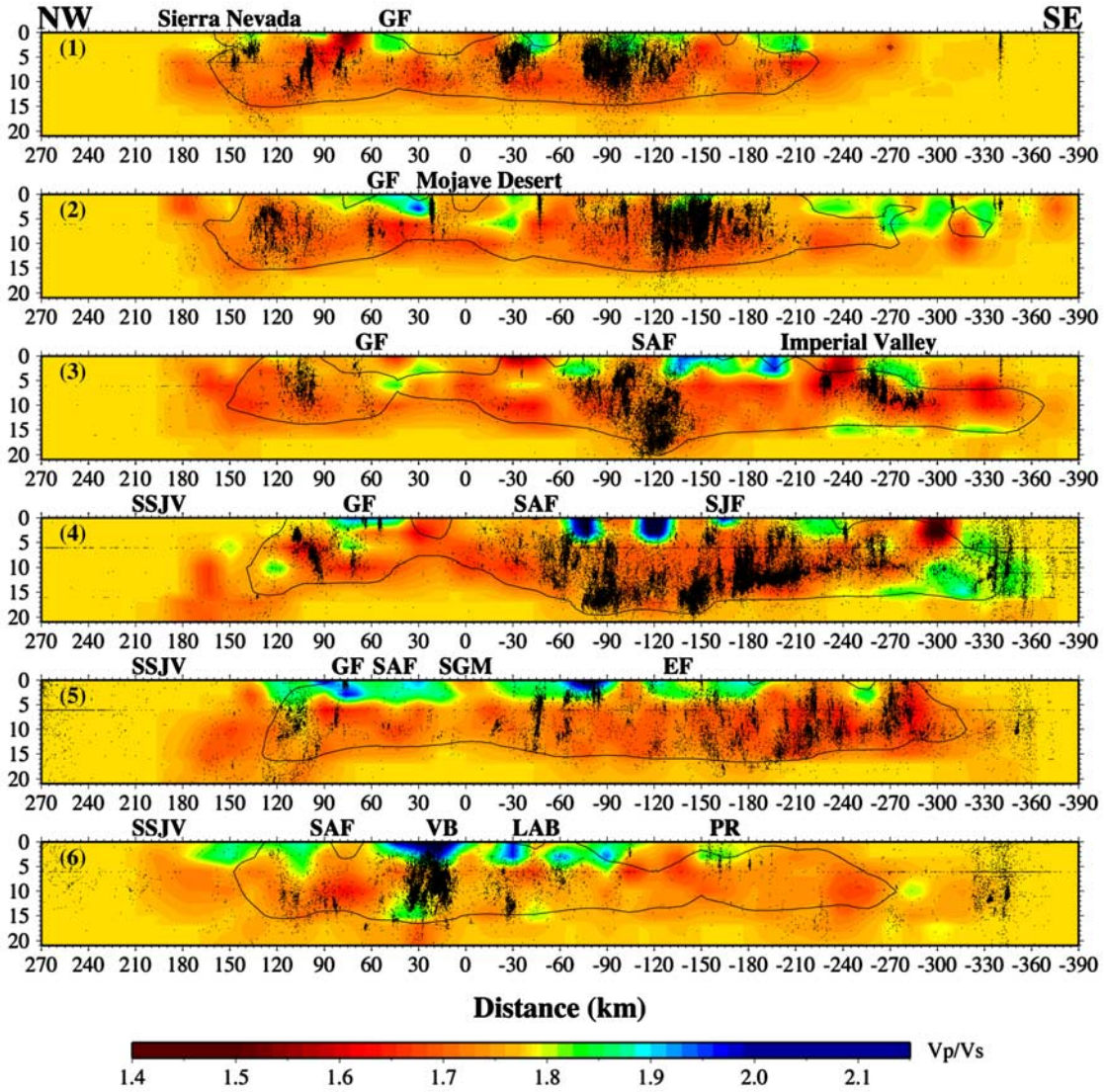

Figure 17. Cross sections through our V_p/V_s model along the NW-SE profiles shown in Figure 12 by numbers, including the background seismicity (black dots) within 10 km distance of the profile line. The black contours enclose the regions with the resolution above 0.1. The vertical exaggeration is 3. The geographical and fault names are the same as in Figure 14.

model. For the 6 and 10 km depth layers, most parts of the well-resolved regions are underlain by lower V_p/V_s values of about 1.71, except that some higher V_p/V_s values are seen in areas along the coast. The resolved areas in the deeper model points (15 and 17 km) are small and have similar patterns as in the V_p model. In the *Hauksson* [2000] model, many high V_p/V_s anomalies are seen below 6 km rather than at the shallower depths where they often occur in our model. These differences are also seen in the cross sections.

[24] In Figures 16 and 17, we plot the cross sections of the V_p/V_s model, and see similar features as in the map view. Although the starting model is 1.78, the resolved areas show average V_p/V_s around 1.73. The basin areas show very high V_p/V_s anomalies near the surface, such as the Ventura Basin, the Los Angeles Basin and the Imperial Valley. We also observe high V_p/V_s blobs beneath some basins in the middle crust, such as the Ventura Basin in profile C and 6, the Los Angeles Basin in D and the Imperial Valley in H and 3. These may be due to the presence of mafic rocks or fluids.

[25] We also used the resulting 3-D velocity model to independently relocate the hypocenters and origin times of the 36 shots used in the inversions. All events have epicenter errors less than 1.5 km, with most errors less than 1.0 km. For the vertical location errors, most are less than 2.0 km. For more details, please refer to *Lin et al.* [2007].

7. Seismicity and Velocity Structure

[26] Figure 18 plots *P* velocity versus depth at the quake locations, compared to the median velocity within the resolved regions of the 3-D model. Focusing first on the velocity model alone, note that the size of the velocity perturbations generally decreases with depth. At shallow depths (<8 km), the low anomalies (associated with the

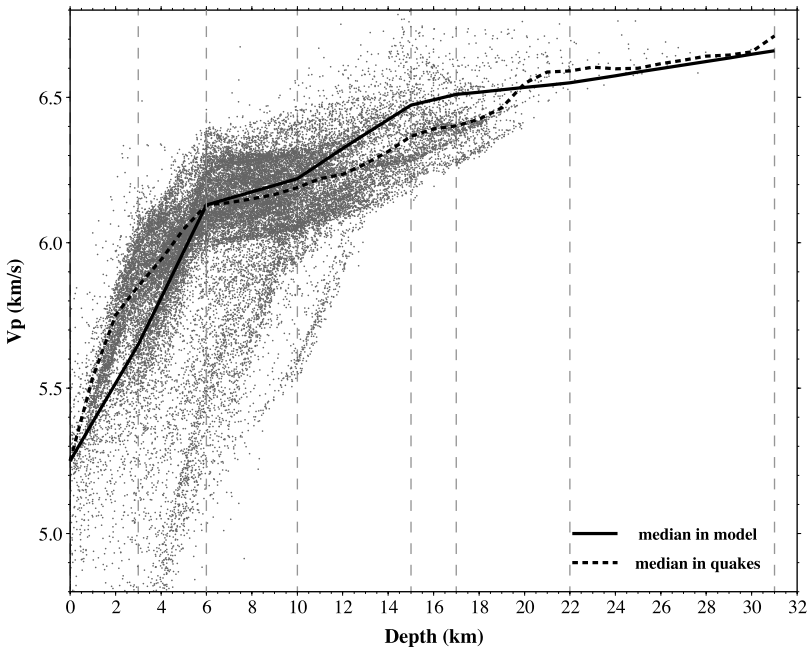

Figure 18. *P* velocity versus depth. Dots are a random 10% of the entire earthquake set. Dashed curve shows the median *P* velocity at the earthquake locations at 1 km depth intervals. For comparison, the solid curve shows the median of the tomography model over all well-resolved grid points.

sedimentary basins) are larger in magnitude than the high anomalies. However, in the lower crust (>14 km) the high-velocity anomalies are larger in magnitude than the low velocity anomalies. The median velocity at the earthquake locations generally tracks the median velocity profile in the 3-D model. However, there are two depth ranges at which the median velocities are significantly different. Between about 1 and 5 km depth, the earthquakes tend to occur more often in rock with higher than average velocity, whereas between about 11 and 18 km, the earthquakes are more

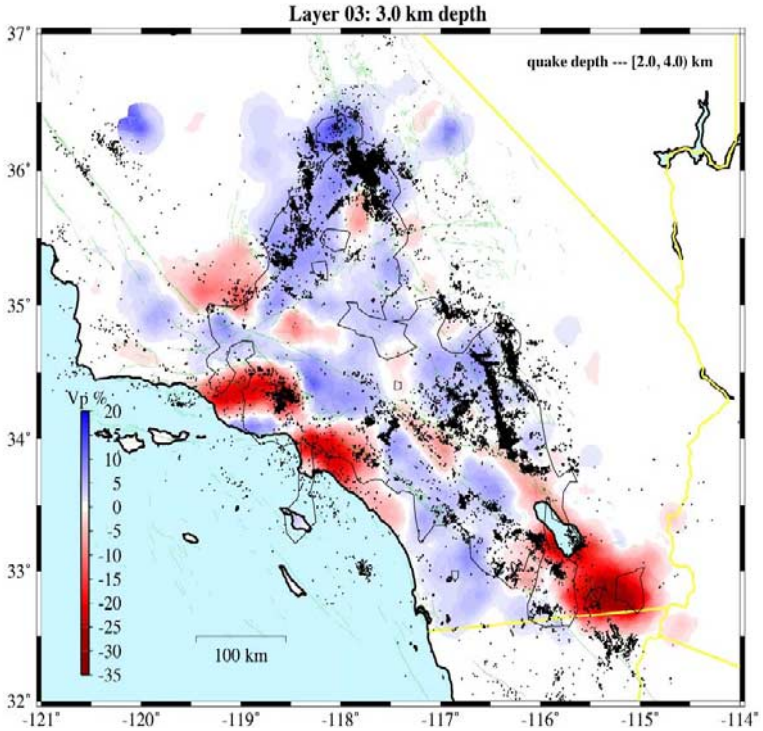

Figure 19. Seismicity between 2 and 4 km depth, compared to *P* velocity perturbations at 3 km. Fast regions are shown in blue, and slow regions are shown in red.

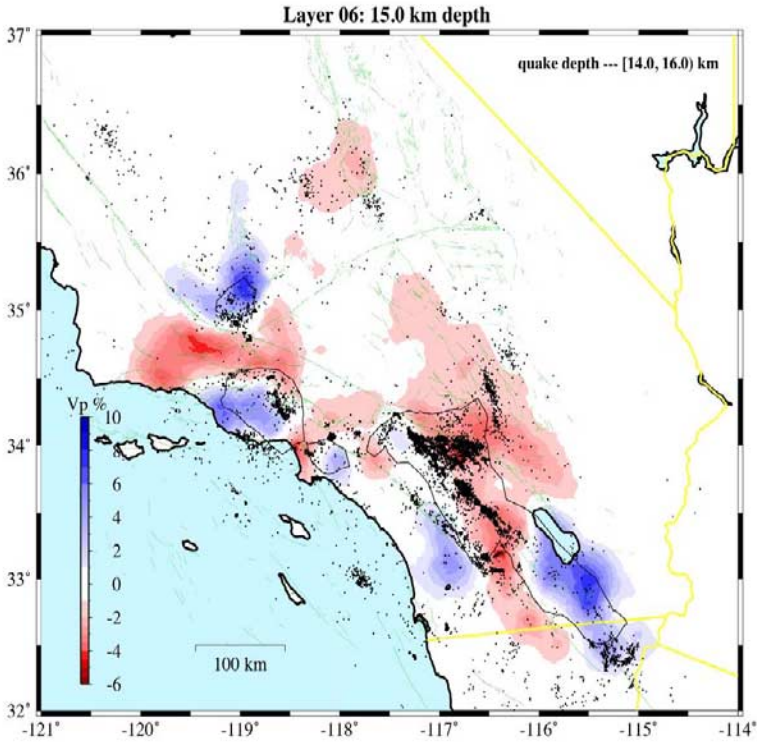

Figure 20. Seismicity between 14 and 16 km depth, compared to *P* velocity perturbations at 15 km. Fast regions are shown in blue, and slow regions are shown in red.

likely to occur in slower than average crust. This pattern can also be seen in Figures 19 and 20, which map the velocity perturbations and the quake locations near 3 km and 15 km depth. Although there are some exceptions (e.g., the shallow Northridge aftershocks), quakes between 2 and 4 km depth tend to occur in the relatively fast hard rock between the sedimentary basins. In contrast, earthquakes between 14 and

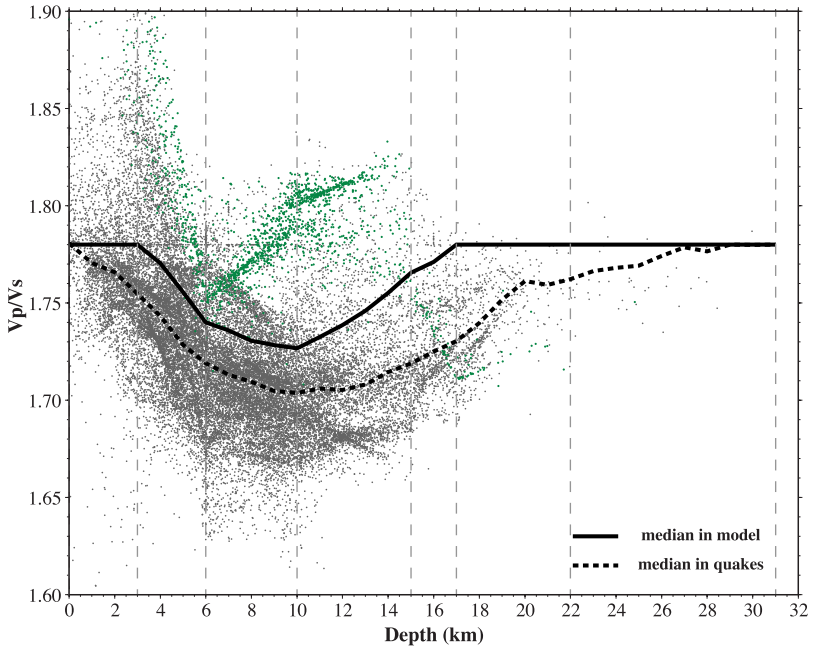

Figure 21. V_p/V_s versus depth. Dots are a random 10% of the entire earthquake set, with the green dots for the 1994 Northridge aftershock sequence (see Figure 22). The dashed curve shows the median V_p/V_s values at the earthquake locations at 1 km depth intervals. For comparison, the solid curve shows the median of the tomography model over all well-resolved grid points.

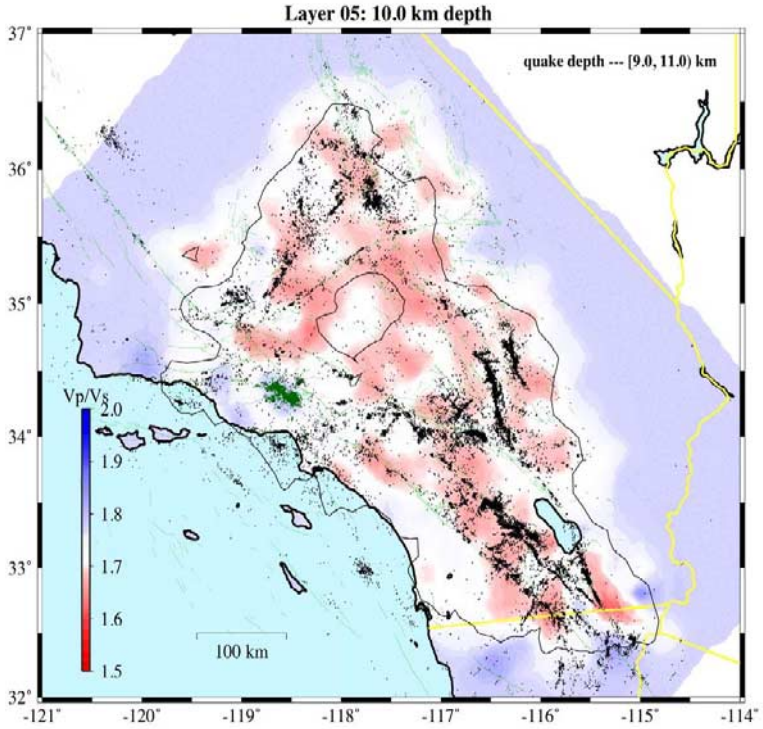

Figure 22. Seismicity between 9 and 11 km depth, compared to the V_p/V_s values at 10 km. High V_p/V_s regions are shown in blue and low V_p/V_s regions in red. The 1994 Northridge aftershock sequence are plotted in green.

16 km are relatively sparse in the highest *P* velocity parts of the model.

[27] We also observe a correlation between earthquake occurrence and lower V_p/V_s values in the midcrust, as shown in Figure 21, which plots the V_p/V_s ratio versus depth at the quake locations, compared to the median value within the resolved regions of the 3-D model. The median V_p/V_s values in the model stay at the starting value of 1.78 in the poorly resolved uppermost 3 km and below 17 km, but approach 1.73 in the best resolved depth range between about 6 and 12 km. At these depths, the earthquakes tend to occur in regions with lower V_p/V_s, with median values of 1.70 to 1.71. There are very few earthquakes in parts of the model with V_p/V_s above about 1.83, an observation similar to results for the 1989 Loma Prieta rupture region [*Thurber et al.*, 1995]. We experimented with using different starting V_p/V_s values for the tomographic inversion and found that the results within the well-resolved depths were relatively insensitive to the starting model, and that the correlation of low V_p/V_s regions with seismicity is a robust result. This correlation can be seen visually in Figure 22, which maps seismicity between 9 and 11 km depth, compared to the V_p/V_s perturbations in the tomography model. The earthquakes tend to avoid the regions with high V_p/V_s ratios, with the notable exception of the major aftershock sequences, such as that following the 1994 Northridge earthquake (shown as the green points in Figures 21 and 22).

[28] An association of seismically active regions with low V_p/V_s ratios is somewhat surprising because one might expect these regions to be more fractured and fluid filled than the surrounding crust, which, in the absence of compositional differences, generally increases the V_p/V_s ratio (an exception is that water-filled cracks with aspect ratios between 2 and 20 can lower V_p/V_s [e.g., *Shearer*, 1988]). Previous studies have obtained varied results concerning the relationship between seismicity and V_p/V_s. *Bannister et al.* [2006] found seismicity at Arthur's Pass, New Zealand, was associated with moderate to slightly low V_p/V_s. *Powell et al.* [2005] detected anomalously low V_p/V_s ratios in the New Madrid Seismic Zone that correlated with major areas of seismicity. However, *Monna et al.* [2003] found aftershock seismicity to mainly occur within a high V_p/V_s region in the central Apennines, Italy, and *Kim and Bae* [2006] computed high V_p/V_s ratios near earthquakes on the Korean peninsula. Because the resolution of our tomography model is very crude compared to the accuracy of the earthquake locations, it is possible that unresolved fine-scale structure in V_p/V_s may be present near seismically active areas that would yield very different V_p/V_s values near the earthquakes themselves. A promising way to study this possibility would be to directly estimate local V_p/V_s ratios within similar event clusters [*Lin and Shearer*, 2007].

8. Discussion

[29] The main features in our model, in particular the low velocities in the sedimentary basins, have been seen in previous regional-scale tomographic models of the southern California crust [e.g., *Magistrale et al.*, 1992; *Tanimoto and Prindle Sheldrake*, 2002; *Zhou*, 2004; *Prindle-Sheldrake and Tanimoto*, 2006]. Our inversion method and the resulting model are most similar to the study by *Hauksson*

[2000]. The two models both resolve low-velocity features at shallow depths in the basins and some high-velocity features in the midcrust. However, the lower crust *P* velocities in our model are slow relative to the values from *Hauksson* [2000]. This is especially obvious in the cross section plots (Figures 13 and 14). Most of the velocities in our model are below 7.0 km/s, while in *Hauksson*'s [2000] study, almost all the profiles show high velocities (above 7.0 km/s) in the lower crust. These differences between the models may be a result of the damping parameters used in the tomographic inversions. We used SIMULPS damping parameters of 800 for the V_p model and 200 for the V_p/V_s model, which are higher than the values used by *Hauksson* [2000] (150 for V_p and 15 for V_p/V_s). As discussed earlier, we used larger damping parameters because we found the data misfit is not as sensitive as the model variance to the damping parameters. After we analyzed the trade-off curves between the data misfits and model variances for both V_p and V_p/V_s, we found that relatively smooth models fit the data almost as well as much rougher models.

[30] Another difference between our model and the *Hauksson* [2000] model is the resolution. We plot the resolution contours in both the map views and the cross sections for our resolved regions with the resolution above 0.1. This resolution is relatively low with respect to the 0.3 resolution contour from *Hauksson* [2000]. In theory, the resolution can be increased by decreasing the damping parameters, but this may result in unreliable velocities. Considering the use of the composite event method, which maximizes the number of available stations for each event, we believe that our model is well resolved. Different starting locations, initial velocity models and parameters used in the tomographic inversions could also cause the differences.

[31] In some parts of southern California, the seismicity and station coverage is good enough that much higher resolution can be achieved in localized regions [e.g., *Lees and Nicholson*, 1993]. The advantage of our model is that it provides uniform resolution across most of southern California and can be used for regional-scale analyses. Although we observe correlations between our model and some of the geological features on the surface, our model generally has poor resolution at shallow depths. In particular, the model overestimates the near-surface velocities in the sedimentary basins. For example, the slowest surface *P* velocity in our model is 3.6 km/s for the San Fernando Valley and 3.7 km/s in the Imperial Valley, whereas seismic refraction results [e.g., *Lutter et al.*, 2004; *Fuis et al.*, 1984] indicate surface velocities of 2.0 and 1.8 km/s, respectively. For earthquakes at depth, there is a trade off between the event origin times and the traveltime increase caused by slow near-surface layers. This trade off is removed to some extent by including the 36 calibration shots of known origin times in the inversion but we have too few of these events to fully cover southern California. In addition, shots often do not produce measurable *S* waves. We have 1349 *P* picks but only 19 *S* picks for the 36 shots. Thus, to obtain more accurate results for the shallow features, it is desirable to incorporate direct constraints on the velocity structure from other geophysical and geological data, an approach recently used by *Magistrale et al.* [2000] in southern California. However, these limitations in our model should not have a significant effect on the resolution of velocity anomalies at depth or for using the model to improve absolute earthquake locations.

[32] **Acknowledgments.** All maps and cross sections in this article were made using the GMT mapping tools. We thank Paul Wessel and Walter Smith for developing and supporting GMT. We also thank the anonymous Associate Editor and the reviewer Toshiro Tanimoto for their detailed and constructive reviews. Funding for this research was provided by NEHRP/USGS grant 03HQPA0001 and the Southern California Earthquake Center, which is funded by NSF Cooperative Agreement EAR-0106924 and USGS Cooperative Agreement 02HQAG0008. Research is also supported in part by the U.S. Geological Survey, Department of the Interior, under USGS awards 06HQGR0055 and 07HQGR0050 to the University of Wisconsin-Madison. The views and conclusions contained in this document are those of the authors and should not be interpreted as necessarily representing the official policies, either expressed or implied, of the U.S. Government. This is SCEC contribution 1050.

References

Bannister, S., C. Thurber, and J. Louie (2006), Detailed fault structure highlighted by finely relocated aftershocks, Arthur's Pass, New Zealand, *Geophys. Res. Lett.*, *33*, L18315, doi:10.1029/2006GL027462.

Dziewonski, A. M. (1984), Mapping the lower mantle: Determination of lateral heterogeneity in P velocity up to degree and order 6, *J. Geophys. Res.*, *89*, 5929–5952.

Eberhart-Phillips, D. (1986), Three-dimensional velocity structure in the northern California Coast Ranges from inversion of local earthquake arrival times, *Bull. Seismol. Soc. Am.*, *76*, 1025–1052.

Eberhart-Phillips, D. (1990), Three-dimensional P and S velocity structure in the Coalinga region, California, *J. Geophys. Res.*, *95*, 15,343–15,363.

Eberhart-Phillips, D. (1993), Local earthquake tomography: earthquake source regions, in *Seismic Tomography: Theory and Practice*, edited by H. M. Iyer and K. Hirahara, pp. 613–643, Chapman and Hall, London.

Evans, J. R., D. Eberhart-Phillips, and C. H. Thurber (1994), User's manual for SIMULPS12 for imaging Vp and Vp/Vs: A derivative of the "Thurber" tomographic inversion SIMUL3 for local earthquakes and explosions, *U.S. Geol. Surv. Open File Rep.*, *94-431*.

Fuis, G. S., W. D. Mooney, J. H. Healy, G. A. McMechan, and W. J. Lutter (1984), A seismic refraction survey of the Imperial Valley region, California, *J. Geophys. Res.*, *89*, 1165–1190.

Gudmundsson, O., J. H. Davies, and R. W. Clayton (1990), Stochastic analysis of global traveltime data: mantle heterogeneity and random errors in the ISC data, *Geophys. J. Int.*, *102*, 25–43.

Hadley, D., and H. Kanamori (1977), Seismic structure of the Transverse Ranges, California, *Geol. Soc. Am. Bull.*, *88*, 1469–1478.

Hauksson, E. (2000), Crustal structure and seismicity distribution adjacent to the Pacific and North America plate boundary in southern California, *J. Geophys. Res.*, *105*, 13,875–13,903.

Kim, S., and H. Bae (2006), Utilizing local tomography to confirm high Vp/Vs ratio discrepancies at hypocenters and partial melting on the Korean Peneisula, *Eos Trans. AGU*, *87*(36), West. Pac. Geophys. Meet. Suppl., Abstract S25A-06.

Kissling, E., W. L. Ellsworth, D. Eberhart-Phillips, and U. Kradolfer (1994), Initial reference models in local earthquake tomography, *J. Geophys. Res.*, *99*, 19,635–19,646.

Lees, J. M., and C. Nicholson (1993), Three-dimensional tomography of the 1992 southern California earthquake sequence: Constraints on dynamic earthquake rupture?, *Geology*, *21*, 387–390.

Lin, G., and P. Shearer (2005), Tests of relative earthquake location techniques using synthetic data, *J. Geophys. Res.*, *110*, B04304, doi:10.1029/2004JB003380.

Lin, G., and P. M. Shearer (2007), Estimating local Vp/Vs ratios within similar earthquake clusters, *Bull. Seismol. Soc. Am.*, *97*, 379–388.

Lin, G., P. M. Shearer, and Y. A. Fialko (2006), Obtaining absolute locations for quarry seismicity using remote sensing data, *Bull. Seismol. Soc. Am.*, *96*, 722–728.

Lin, G., P. M. Shearer, and E. Hauksson (2007), Applying three-dimensional velocity models, waveform cross-correlation, and clustering to relocate the southern California seismicity from 1981 to 2005, *J. Geophys. Res.*, doi:10.1029/2007JB004986, in press.

Lutter, W. J., et al. (2004), Upper crustal structure from the Santa Monica Mountains to the Sierra Nevada, southern Californnia: Tomographic results from the Los Angeles regional seismic experiment, phase II (LARSE II), *Bull. Seismol. Soc. Am.*, *94*, 619–632.

Magistrale, H., H. Kanamori, and C. Jones (1992), Forward and inverse three-dimensional P wave velocity models of the southern California crust, *J. Geophys. Res.*, *97*, 14,115–14,135.

Magistrale, H., S. Day, R. W. Clayton, and R. Graves (2000), The SCEC southern California reference three-dimensional seismic velocity model version 2, *Bull. Seismol. Soc. Am.*, *90*, S65–S76.

Monna, S., L. Filippi, L. Beranzoli, and P. Favali (2003), Rock properties of the upper-crust in Central Apennines (Italy) derived from high-resolution 3-D tomography, *Geophys. Res. Lett.*, *30*(7), 1408, doi:10.1029/2002GL016780.

Pavlis, G. L., and J. R. Booker (1980), The mixed discrete-continuous inverse problem: application to the simultaneous determination of earthquake hypocenters and velocity structure, *J. Geophys. Res.*, *85*, 4801–4810.

Powell, C., M. Withers, M. Dunn, and G. Vlahovic (2005), Anomalous Vp/Vs ratios in the New Madrid seismic zone: Implications for seismic hazard mapping, *Seismol. Res. Lett.*, *77*, 107–108.

Prindle-Sheldrake, K., and T. Tanimoto (2006), Teleseismic surface wave study for *S*-wave velocity structure under an array: Southern California, *Geophys. J. Int.*, *166*, 601–621.

Richards-Dinger, K. B., and P. M. Shearer (2000), Earthquake locations in southern California obtained using source-specific station terms, *J. Geophys. Res.*, *105*, 10,939–10,960.

Shearer, P. M. (1988), Cracked media, Poisson's ratio, and the structure of the upper oceanic crust, *Geophys. J.*, *92*, 357–362.

Shearer, P. M., E. Hauksson, and G. Lin (2005), Southern California hypocenter relocation with waveform cross-correlation, part 2: Results using source-specific station terms and cluster analysis, *Bull. Seismol. Soc. Am.*, *95*, 904–915.

Spakman, W., and H. Bijwaard (2001), Optimization of cell parameterizations for tomographic inverse problems, *Pure Appl. Geophys.*, *158*, 1401–1423.

Spencer, C., and D. Gubbins (1980), Travel-time inversion for simultaneous earthquake location and velocity structure determination in laterally varying media, *Geophys. J. R. Astron. Soc.*, *63*, 95–116.

Tanimoto, T., and K. Prindle Sheldrake (2002), Three-dimensional S-wave velocity structure in Southern California, *Geophys. Res. Lett.*, *29*(8), 1223, doi:10.1029/2001GL013486.

Thurber, C. H. (1983), Earthquake locations and three-dimensional crustal structure in the Coyote Lake area, central California, *J. Geophys. Res.*, *88*, 8226–8236.

Thurber, C. H. (1993), Local earthquake tomography: velocities and Vp/Vs-theory, in *Seismic Tomogrphy: Theory and Practice*, edited by H. M. Iyer and K. Hirahara, pp. 563–583, Chapman and Hall, London.

Thurber, C. H., S. R. Atre, and D. Eberhart-Phillips (1995), Three-dimensional Vp and Vp/Vs structure at Loma Prieta, California, from local earthquake tomography, *Geophys. Res. Lett.*, *22*, 3079–3082.

Zhang, H., C. Thurber, T. Brocher, Y. Liu, and C. Evangelidis (2006), A new regional seismic tomography model for northern California, *Seismol. Res. Lett.*, *77*, 271.

Zhou, H.-W. (2004), Multi-scale tomography for crustal *P* and *S* velocities in southern California, *Pure Appl. Geophys.*, *161*, 283–302.

Zhu, L., and H. Kanamori (2000), Moho depth variation in southern California from teleseismic receiver functions, *J. Geophys. Res.*, *105*, 2969–2980.

E. Hauksson, Seismological Laboratory, MS 252-21, California Institute of Technology, Pasadena, CA 91125, USA. (hauksson@gps.caltech.edu)

G. Lin and C. H. Thurber, Department of Geology and Geophysics, University of Wisconsin-Madison, Madison, WI 53706, USA. (glin@geology.wisc.edu; thurber@geology.wisc.edu)

P. M. Shearer, Institute of Geophysics and Planetary Physics, Scripps Institution of Oceanography, University of California San Diego, La Jolla, CA 92093, USA. (pshearer@ucsd.edu)